High-stability dead-end anode proton exchange membrane fuel cells by purge optimization

Jing Yao[a], Zhen Wu[a,*], Bofei Wang[a], Yuchen Yang[a], Fusheng Yang[a], Zaoxiao Zhang[a,b,*], Jianwei Ren[c], Bo Li[d]

[a] *School of Chemical Engineering and Technology, Xi'an Jiaotong University, Xi'an, 710049, PR China*

[b] *State Key Laboratory of Multiphase Flow in Power Engineering, Xi'an Jiaotong University, Xi'an, 710049, PR China*

[c] *Department of Mechanical Engineering Science, University of Johannesburg, Johannesburg, 2092, South Africa*

[d] *School of Engineering, University of Kent, Kent, CT2 7NZ, UK*

** Corresponding author, E-mail address: wuz2015@mail.xjtu.edu.cn (Z. Wu), zhangzx@mail.xjtu.edu.cn (Z Zhang).*

Abstract

The crossover of nitrogen and oxygen from cathode to anode aggravates the non-uniformity inside dead-end anode proton exchange membrane fuel cell (DEA-PEMFC), inducing some other effects, such as carbon corrosion, to cause irreversible damage to catalyst. Therefore, developing a purge strategy according to the non-uniformity is necessary to improve its stability. In this study, the effects of operating parameters on the uneven electrical-thermal-water performance are investigated based on a three-dimensional transient model of DEA-PEMFC. Afterwards, a purge optimization is carried out based on the uneven distribution of field variables. The results show that the calculated standard deviation (*STDEV*) of overvoltage is reduced first and then increased quickly for all the cases. Therefore, the purge should be started when the *STDEV* approaches the minimum value, to avoid the irreversible damage to DEA-PEMFC, achieving high-stability output performance meanwhile. On this basis, the purge interval is optimized to 100 s, which is suitable for almost all the discussed cases. The purge duration is reduced to 0.2 s. In this situation, the minimum voltage is decreased by about 0.95% compared with the maximum value, indicating a good voltage stability. This study is beneficial to provide guidance for the efficient and long-term operation of DEA-PEMFC.

Keywords: *Proton exchange membrane fuel cell; Dead-end anode; Electrical-thermal-water performance; Multi-phase model; Purge strategy*

1 Introduction

Fossil fuels are employed as the main energy sources for a long time [1]. However, the drawbacks brought by fossil fuel combustion are gradually becoming prominent [2]. Therefore, the development of renewable energy is of great importance. Among all kinds of available renewable energies, hydrogen energy is regarded as one of the most promising secondary energy sources in the future due to its high heating value and zero-emission [3].

Fuel cell is the key device for the conversion and utilization of hydrogen energy. According to the electrolyte material, fuel cell could be categorized into five types: polymer electrolyte membrane or proton exchange membrane fuel cell (PEMFC), alkaline fuel cell, phosphoric acid fuel cell, molten carbonate fuel cell, and solid oxide fuel cell [4]. PEMFC is considered as the most potential one due to its mild operating conditions, fast start-up, high stability, and simple structure [5].

To achieve the high utilization of hydrogen gas in practice, two modes are generally used at the anode of PEMFC: flow-through anode (FTA) mode and dead-end anode (DEA) mode [6]. At the FTA mode, excess hydrogen gas flows through the anode directly. In the meanwhile, to avoid hydrogen waste, hydrogen recirculation should be equipped at the anode [7]. This kind of mode is suitable for the PEMFC with large power considering the complexity of the hydrogen recirculation device. At the DEA mode, the anode outlet of PEMFC is closed with a valve. Therefore, all the hydrogen entering from the inlet is consumed, thereby the hydrogen utilization achieves high [8]. DEA mode is generally applied in the air-cooled PEMFC with relatively small power (< 2 kW). Meanwhile, this mode also helps to reduce the device complexity, thus to improve the energy density of PEMFC [9]. However, DEA mode could also result in the performance degradation of PEMFC which has been observed in experiments [10]. Some studies indicated that the accumulation of liquid water and impurities at the anode is the main reason [11]. The liquid water at the anode would block the pore to prevent the contact between hydrogen gas and catalyst. Besides, the impurities (N_2 and O_2) transferred from cathode to anode could reduce the hydrogen concentration for electrochemical reaction. It is also worth noting that, according to Manokaran et al. [12], nitrogen is the major contributor to performance drop when air is used as oxidant.

To restore the performance of dead-end anode proton exchange membrane fuel cell (DEA-PEMFC), purge is regarded as an effective method to clear the liquid water and impurities at the anode [13]. The previous studies have paid much attention to the purge process. Jian et al. [14] experimentally optimized the purge strategy of an air-cooled DEA-PEMFC, giving attention to both hydrogen utilization and voltage stability. The optimal purge interval of 14.86 s and purge duration of 0.44 s are obtained. Sasmito et al. [15] employed full factorial approach to develop a better understanding of the interactions between the purge parameters and the cathode stoichiometry ratio for a DEA-PEMFC with the rated power of 1500 W. Also, the optimal parameters are obtained: purge interval of 180 s, purge duration of 4 s, and cathode stoichiometry ratio of 2. Hu et al. [16] performed experiments under different purge strategies. The results showed that under the optimal purge strategy, DEA-PEMFC is able to achieve the desired stability and the system efficiency of more than 92%. Besides, it is also found that the purge valve with the diameter of 3 mm enables to achieve better voltage stability than that with the diameter of 1.6 mm. In addition, Shen et al. [17] focused on the purge effects on the dynamic performance of dual DEA-PEMFC stacks. They also

proposed a novel gas supply configuration to improve hydrogen utilization during the purge process for dual DEA-PEMFC stacks [18]. The optimized series configuration prolongs the purge interval from 125 s to 800 s, and thus increases the hydrogen utilization from 97.51% to 99.21%.

In addition, the investigators have developed plenty of numerical models to study the purge process of DEA-PEMFC. Wang et al. [19] developed a quasi-two-dimensional transient model to optimize the purge strategy. The effects of the purge parameters, including purge interval, scavenging velocity, and purge duration, on the DEA-PEMFC were studied for performance optimization. It's also worth mentioning that this study discussed both the voltage-based purge and nitrogen-based purge. Nevertheless, considering the difficulty of the in-situ and real-time nitrogen fraction measurement, voltage-based purge is recommended for practical application. Chen et al. [20] developed a three-dimensional model of DEA-PEMFC. The effects of operating conditions on the performance were investigated. Meanwhile, the corresponding purge strategy was optimized. The results showed that the purge duration of 10 ms is the optimal value for base case, achieving the hydrogen utilization of 95.47%.

Although these studies aim at the optimization of purge strategy, the motivation for determining the purge interval mainly comes from the superficial voltage drop, duration, or impurity concentration. In other words, the internal information of DEA-PEMFC is not used to determine the purge strategy. In fact, relatively large non-uniformity has been observed in PEMFC due to the uneven distribution of reactants [21, 22]. As for DEA-PEMFC, the crossover of nitrogen and oxygen would aggravate the non-uniformity of variables [23]. It should be noted that the non-uniformity is potential to induce some other effects, such as carbon corrosion, which would cause irreversible damage to DEA-PEMFC [24]. This phenomenon is unbeneficial to the long-term service of DEA-PEMFC. Therefore, it is reasonable to carry out a purge optimization according to the uneven distribution of field variables inside DEA-PEMFC, to improve the stability of DEA-PEMFC.

In this study, a three-dimensional transient model of DEA-PEMFC integrated with the crossover of nitrogen and oxygen is developed to describe the internal species transport behaviors and electrochemical reaction process. Then, the effects of operating parameters, including current density, operating temperature, and cathode stoichiometry ratio at the cathode, on the uneven electrical-thermal-water performance are investigated. Finally, a purge optimization is carried out based on the uneven distribution of field variables to achieve the high stability of DEA-PEMFC.

2 Methods

The schematic diagram of a DEA-PEMFC is presented in Fig. 1. At the anode, hydrogen diffuses from gas channel to catalyst layer (CL), passing through gas diffusion layer (GDL). Then, hydrogen is oxidized to proton at the CL. Afterwards, the generated proton is transferred to cathode through the membrane. Meanwhile, to improve the utilization of hydrogen, a solenoid valve is installed at the outlet of anode channel to control the outlet state. At the cathode, oxygen is reduced at the CL, and then combined with the proton to produce water. Due to the low temperature requirement for DEA-PEMFC, on the one hand, the heat dissipation in the DEA-PEMFC should be paid much attention to prevent the irreversible structural damage. On the other hand, the liquid water introduced by

low temperature is proven to affect the electrochemical reaction performance significantly. Therefore, the electrical-thermal-water performance of a DEA-PEMFC is comprehensively analysed in this study. The non-uniformity of variables is described with standard deviation (*STDEV*), as written in Eq. (1).

$$STDEV = \sqrt{\frac{\left(x_1 - \bar{x}\right)^2 + \left(x_2 - \bar{x}\right)^2 + \cdots + \left(x_n - \bar{x}\right)^2}{n}} \tag{1}$$

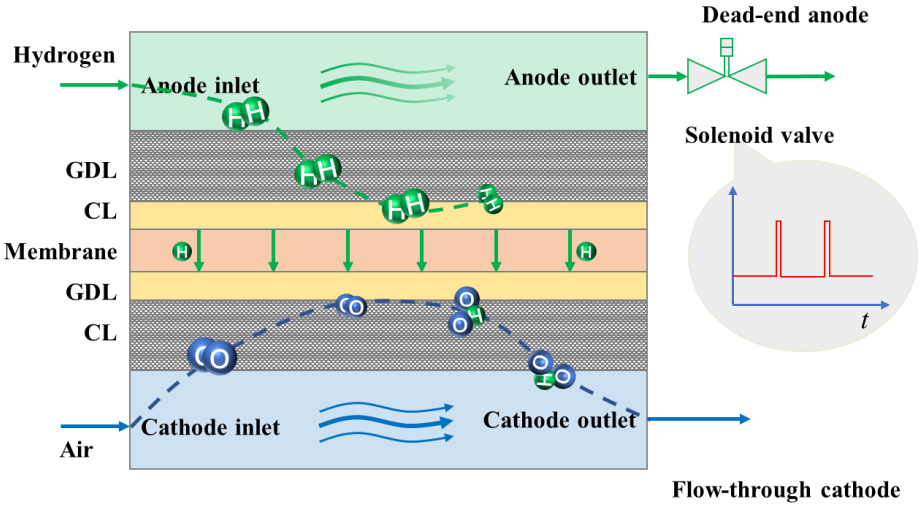

Fig. 1. The schematic diagram of a DEA-PEMFC.

Due to anode outlet is close for most of the time, the physical field distribution inside DEA-PEMFC varies over time. Therefore, a transient 3D non-isothermal multi-phase model is developed to describe the heat and mass transfer behaviours and to obtain the corresponding electrical-thermal-water performance.

2.1 Model assumptions

PEMFC is a complex reaction device, involving multiple components and the coupling of multiple physical fields. To simplify the calculation, the following assumptions are made:

(1) The effects of gravity on the fluid flow are negligible;

(2) The gas phase is in the laminar flow state due to the low velocity [25];

(3) The gases at the anode and the cathode are treated as ideal gas due to the relatively low pressure and temperature [26];

(4) The porous media including GDL and CL are considered to be homogenous;

(5) The membrane is impermeable for electrons, while it is permeable for dissolved water and protons;

(6) The liquid water is assumed to be in the mist state [27];

(7) The water generated by the electrochemical reaction at the cathode is assumed to be in the form of dissolved water [28].

2.2 Governing equations

The model of DEA-PEMFC mainly includes 12 equations, as seen in Table 1 [29-31].

Table 1. Governing equations for DEA-PEMFC model [29-31].

Equation	Expression
Mass conservation equation	$\frac{\partial(\varepsilon\rho_{\mathrm{g}})}{\partial t}+\nabla\bullet(\rho_{\mathrm{g}}\vec{u}_{\mathrm{g}})=S_{\mathrm{m}}$
Momentum conservation equation (for three directions)	$\frac{\partial}{\partial t}(\frac{\rho_{\mathrm{g}}\vec{u}_{\mathrm{g}}}{\varepsilon})+\nabla\bullet(\frac{\rho_{\mathrm{g}}\vec{u}_{\mathrm{g}}\vec{u}_{\mathrm{g}}}{\varepsilon^2})=-\nabla P_{\mathrm{g}}+\nabla\bullet(\frac{\mu_{\mathrm{g}}}{\varepsilon}((\nabla\vec{u}_{\mathrm{g}}+\nabla\vec{u}_{\mathrm{g}}{}^{\mathrm{T}})-\frac{2}{3}\nabla\bullet\vec{u}_{\mathrm{g}}))+S_{\mathrm{u}}$
Species transport equation (for H_2, O_2, and H_2O)	$\frac{\partial(\varepsilon\rho_{\mathrm{g}}w_i)}{\partial t}+\nabla\bullet(\rho_{\mathrm{g}}\vec{u}_{\mathrm{g}}w_i)=\nabla\bullet(\rho_{\mathrm{g}}D_{i,\mathrm{eff}}\nabla w_i)+S_i$
Energy conservation equation	$\frac{\partial}{\partial t}((\varepsilon\rho_{\mathrm{g}}C_{p,\mathrm{g}}+(1-\varepsilon)\rho_{\mathrm{s}}C_{p,\mathrm{s}})T)+\nabla\bullet(\vec{u}_{\mathrm{g}}\rho_{\mathrm{g}}C_{p,\mathrm{g}}T)=\nabla\bullet(k_{T,\mathrm{eff}}\nabla T)+S_{\mathrm{T}}$
Electronic charge conservation equation	$0=\nabla\bullet(\sigma_{\mathrm{ele}}\nabla\phi_{\mathrm{ele}})+S_{\mathrm{ele}}$
Ionic charge conservation equation	$0=\nabla\bullet(\sigma_{\mathrm{ion}}\nabla\phi_{\mathrm{ion}})+S_{\mathrm{ion}}$
Dissolved water transport equation	$\frac{\rho_{\mathrm{mem}}}{EW}\frac{\partial(\omega\lambda)}{\partial t}+\nabla\bullet(n_d\frac{J_{\mathrm{ion}}}{F})=\frac{\rho_{\mathrm{mem}}}{EW}\nabla\bullet(D_{\mathrm{d,eff}}\nabla\lambda)+S_{\mathrm{w,d}}$
Liquid water transport equation	$\frac{\partial}{\partial t}(\varepsilon\rho_{\mathrm{l}}s)+\nabla\bullet(f(s)\rho_{\mathrm{l}}\vec{u})=\nabla\bullet(\rho_{\mathrm{l}}D_{\mathrm{l}}\nabla s)+S_{\mathrm{w,l}}$

In DEA-PEMFC, water exists in the form of three phases: vapor, dissolved water, and liquid water. The phase change of water is displayed in Fig. S1. In this model, vapor distribution is obtained by solving the corresponding species transport equation. The effective diffusion coefficient (m^2/s) for species transport equation is expressed as Eq. (2) [32].

$$D_{i,\text{eff}} = D_i \varepsilon^{1.5} (1-s)^{1.5} \left(\frac{T}{333.15} \right)^{1.5} \frac{101325}{P} \tag{2}$$

For the dissolved water, its transport equation (as seen in Table 1) is solved in the domain of CL and membrane. The first term on the left is the unsteady term. The second term on the left denotes the dissolved water transport by electro-osmotic drag force. Correspondingly, the electro-osmotic drag coefficient is written as Eq. (3) [33]. The first term on the right is the diffusion term. The diffusivity coefficient (m^2/s) is expressed as Eq. (4) [34]. The second term on the right is the source term.

$$n_d = \frac{2.5}{22} \lambda \tag{3}$$

$$D_{\text{d,eff}} = \begin{cases} 3.1\times10^{-7} \lambda (\exp(0.28\lambda) - 1) \exp(-2346/T) & 0 < \lambda < 3 \\ 4.17\times10^{-8} \lambda (161\exp(-\lambda) + 1) \exp(-2346/T) & 3 \le \lambda < 17 \\ 4.1\times10^{-10} (\lambda/25)^{0.15} (1 + \tanh((\lambda - 2.5)/1.4)) & \lambda \ge 17 \end{cases} \tag{4}$$

Besides, liquid water is presented by liquid water saturation s, which denotes its volume fraction [35]. For the convection term of liquid water transport equation, the interfacial drag coefficient $f(s)$ is written as Eq. (5). For the diffusion term, the diffusivity of liquid water saturation D_l (m^2/s) is expressed as Eq. (6).

$$f(s) = \frac{k_{r,\text{l}}}{k_{r,\text{g}}} \frac{\mu_\text{g}}{\mu_\text{l}} \tag{5}$$

where $k_{r,\text{l}}$ denotes the relative permeability of liquid water; $k_{r,\text{g}}$ denotes the relative permeability of gas.

$$D_\text{l} = -\frac{k_\text{p} k_{r,\text{l}}}{\mu_\text{l}} \frac{dP_\text{cap}}{ds} \tag{6}$$

where k_p is the permeability (m^2); P_cap is the capillary pressure (Pa), expressed as Eq. (7).

$$P_\text{cap} = \sigma_t \cos(\theta_\text{c}) \left(\frac{\varepsilon}{k_\text{p}} \right)^{0.5} J(s) \tag{7}$$

where σ_t is the surface tension (N/m); θ_c is the contact angle ($^\circ$); $J(s)$ is the Leverett-J function, expressed in Eq. (8).

$$J(s) = \begin{cases} 1.417(1-s) - 2.120(1-s)^2 + 1.263(1-s)^3 & \theta_\text{c} < 90^\circ \\ 1.417s - 2.120s^2 + 1.263s^3 & \theta_\text{c} > 90^\circ \end{cases} \tag{8}$$

2.3 Agglomerate model

To finely describe the electrochemical reaction and species transport in the CL, agglomerate model is also integrated in this model. In the agglomerate model, the CL is considered to be composed of a large number of agglomerates. Each agglomerate could be viewed as a cluster of carbon particles with catalyst dispersed on the surface. These agglomerates are coated with a thin ionomer film and connected by ionomer network [36].

The agglomerate model could be used to determine the properties at both the macro level and the micro level [29]. At the macro level, the sum of the volume fraction of each part in the CL is equal to 1.0, expressed as Eq. (9).

$$L_{\text{Ionomer}} + L_{\text{Pt/C}} + L_{\text{GDL}} + \varepsilon_{\text{CL}} = 1 \tag{9}$$

where L_{Ionomer} is the volume fraction of ionomer, written as Eq. (10); $L_{\text{Pt/C}}$ is the volume fraction of platinum dispersed carbon, written as Eq. (11); L_{GDL} is the volume fraction of GDL penetration; ε_{CL} is the porosity of the CL.

$$L_{\text{Ionomer}} = \left(1 + k_{\text{swe}}\lambda\right) L_{\text{Ionomer,dry}} \tag{10}$$

where k_{swe} is the membrane swelling coefficient; $L_{\text{Ionomer,dry}}$ is the volume fraction of dry ionomer.

$$L_{\text{Pt/C}} = \frac{1}{\delta_{\text{CL}}}\left(\frac{m_{\text{Pt}}}{\rho_{\text{Pt}}} + \frac{m_{\text{C}}}{\rho_{\text{C}}}\right) \tag{11}$$

where m_{Pt} is the platinum loading (mg/cm^2); m_{C} is the carbon loading (mg/cm^2).

Therefore, the porosity of the CL is given as Eq. (12).

$$\varepsilon_{\text{CL}} = 1 - L_{\text{Ionomer}} - L_{\text{Pt/C}} - L_{\text{GDL}} \tag{12}$$

At the micro level, the agglomerate density (i.e., number of agglomerates per unit volume of CL, 1/m^3) is written as Eq. (13). Then, the specific area of agglomerate (1/m) could be written as Eq. (14).

$$N_{\text{agg}} = \frac{3L_{\text{Pt/C}}}{4\left(1-\varepsilon_{\text{CL}}\right)\pi r_{\text{agg}}^3} \tag{13}$$

where r_{agg} is the agglomerate radius (m).

$$a_{\text{agg}} = \frac{3m_{\text{Pt}}A_{\text{rea}}}{4\pi\delta_{\text{CL}}N_{\text{agg}}r_{\text{agg}}^3} \tag{14}$$

where A_{rea} is the reaction area per unit platinum mass (m^2/kg), as expressed in Eq. (15) [37].

$$A_{\mathrm{rea}} = \left(227.79 f^3 - 158.57 f^2 - 201.53 f + 159.5\right) \times 10^3 \tag{15}$$

where f is the platinum mass ratio.

At the same time, the thickness of ionomer film (m) covering the agglomerate is given as Eq. (16). The thickness of liquid water coating (m) is expressed as Eq. (17) [38].

$$\delta_{\mathrm{Ionomer}} = r_{\mathrm{agg}} \left(\sqrt[3]{\frac{\left(1-\varepsilon_{\mathrm{CL}}\right)\left(1-\varepsilon_{\mathrm{CL}}-L_{\mathrm{GDL}}\right)+L_{\mathrm{Pt/C}}\varepsilon_{\mathrm{CL}}\left(1-BM\right)}{L_{\mathrm{Pt/C}}}} - 1 \right) \tag{16}$$

where BM denotes the volume fraction of the primary pores occupied by the ionomer in the agglomerate.

$$\delta_{\mathrm{w,l}} = \sqrt[3]{\left(r_{\mathrm{agg}}+\delta_{\mathrm{Ionomer}}\right)^3 + \frac{s\varepsilon_{\mathrm{CL}}\left(1-\varepsilon_{\mathrm{CL}}\right)r_{\mathrm{agg}}^3}{L_{\mathrm{Pt/C}}}} - \left(r_{\mathrm{agg}}+\delta_{\mathrm{Ionomer}}\right) \tag{17}$$

2.4 Electrochemical reaction kinetics

Based on the agglomerate model, the electrochemical reaction kinetic (A/m^3) at the cathode is modified, in order to consider the impact of liquid water and ionomer film on the species transport, expressed as Eq. (18) [39].

$$i_{\mathrm{c}} = 4F \frac{P_{\mathrm{O_2}}}{H_{\mathrm{O_2}}} \left(\frac{1}{E_{\mathrm{agg}} k_{\mathrm{agg}}} + \frac{r_{\mathrm{agg}}+\delta}{\gamma r_{\mathrm{agg}}} \right)^{-1} \tag{18}$$

where $H_{\mathrm{O_2}}$ is the Henry's constant of oxygen (Pa m^3/mol); E_{agg} is the effectiveness factor of the agglomerate; k_{agg} is the reaction rate coefficient (1/s), expressed as Eq. (19); δ is the total thickness of the ionomer and liquid water film (m); γ is the oxygen diffusion rate through the ionomer/liquid water film (1/s).

$$k_{\mathrm{agg}} = \frac{a_{\mathrm{agg}}}{4F} \frac{i_{\mathrm{c,ref}}}{c_{\mathrm{O_2,ref}}} \left(\exp\left(\frac{-\alpha_{\mathrm{c}} F \eta_c}{RT}\right) - \exp\left(\frac{\left(1-\alpha_{\mathrm{c}}\right) F \eta_c}{RT}\right) \right) \tag{19}$$

where $i_{\mathrm{c,ref}}$ is the reference exchange current density at the cathode (A/m^2); $c_{\mathrm{O_2,ref}}$ is the reference oxygen concentration (mol/m^3); α_{c} is the charge transfer coefficient at the cathode; η_c is the cathode overpotential (V), given as Eq. (20).

$$\eta_{\mathrm{c}} = \phi_{\mathrm{ele}} - \phi_{\mathrm{ion}} - E_{\mathrm{eq,c}} \tag{20}$$

where $E_{\mathrm{eq,c}}$ is the equilibrium potential of cathode (V).

At the anode, the electrochemical reaction kinetics (A/m^3) is given as Butler-Volmer equation, shown in Eq. (21).

$$i_{\mathrm{a}} = a_{\mathrm{agg}} i_{\mathrm{a,ref}} \left(\frac{P_{\mathrm{H_2}}}{c_{\mathrm{H_2,ref}} H_{\mathrm{H_2}}} \right)^{0.5} \left(\exp\left(\frac{(1-\alpha_{\mathrm{a}}) F \eta_{\mathrm{a}}}{RT} \right) - \exp\left(\frac{\alpha_{\mathrm{a}} F \eta_{\mathrm{a}}}{RT} \right) \right) \tag{21}$$

where $i_{\mathrm{a,ref}}$ is the reference exchange current density at the anode (A/m^2); $c_{\mathrm{H_2,ref}}$ is the reference hydrogen concentration (mol/m^3); $H_{\mathrm{H_2}}$ is the Henry's constant of hydrogen (Pa m^3/mol); α_{a} is the charge transfer coefficient at the anode; η_{a} is the anode overpotential (V), given as Eq. (22).

$$\eta_{\mathrm{a}} = \phi_{\mathrm{ele}} - \phi_{\mathrm{ion}} - E_{\mathrm{eq,a}} \tag{22}$$

where $E_{\mathrm{eq,a}}$ is the equilibrium potential of anode (V).

2.5 Crossover of nitrogen and oxygen

Considering that the proton exchange membrane is permeable to nitrogen and oxygen, and that the anode outlet is closed, DEA mode is easy to cause the accumulation of impurities at the anode. Previous studies have proven that the accumulation of nitrogen and oxygen would reduce the hydrogen concentration participating in the electrochemical reaction at the anode CL, leading to the significant performance degradation [40]. Therefore, the crossover of nitrogen and oxygen is added in this model.

The difference of partial pressure between cathode and anode is considered as the driving force for species transport. Therefore, the nitrogen and oxygen fluxes (mol/m^2/s) through the membrane are given as Eqs. (23-24).

$$J_{\mathrm{N_2}} = k_{\mathrm{p,N_2}} \frac{\left(P_{\mathrm{N_2,c}} - P_{\mathrm{N_2,a}} \right)}{\delta_{\mathrm{mem}}} \tag{23}$$

$$J_{\mathrm{O_2}} = k_{\mathrm{p,O_2}} \frac{\left(P_{\mathrm{O_2,c}} - P_{\mathrm{O_2,a}} \right)}{\delta_{\mathrm{mem}}} \tag{24}$$

where $k_{\mathrm{p,N_2}}$ and $k_{\mathrm{p,O_2}}$ are the permeability of nitrogen and oxygen (mol/m/s/Pa), respectively.

The permeability of nitrogen and oxygen is written in Eqs. (25-26) [41].

$$k_{\mathrm{p,N_2}} = \left(0.0295 + 1.21 f_{\mathrm{v}} - 1.93 f_{\mathrm{v}}^{\,2} \right) \times 10^{-14} \exp\left(\frac{E_{\mathrm{N_2}}}{R} \left(\frac{1}{T_{\mathrm{ref}}} - \frac{1}{T} \right) \right) \tag{25}$$

$$k_{\mathrm{p,O_2}} = \left(0.11 + 1.9 f_{\mathrm{v}} \right) \times 10^{-14} \exp\left(\frac{E_{\mathrm{O_2}}}{R} \left(\frac{1}{T_{\mathrm{ref}}} - \frac{1}{T} \right) \right) \tag{26}$$

where f_v denotes the volume fraction of dissolved water, written as Eq. (27); E_{N_2} is the activation energy of nitrogen, 24000 J/mol; T_{ref} is the reference temperature, 303 K; E_{O_2} is the activation energy of oxygen, 20000 J/mol.

$$f_v = \frac{\lambda_{mem} V_{w,l}}{V_{mem} + \lambda_{mem} V_{w,l}} \tag{27}$$

where $V_{w,l}$ and V_{mem} are the mole volumes of liquid water and dry membrane (m^3/mol).

The nitrogen and oxygen fluxes are calculated using variables in different regions, which could be hard to implement in the numerical model. For simplicity, the fluxes are converted to a mass source term added at the anode CL in this model. Besides, the decrease of nitrogen and oxygen concentration at the cathode is neglected, because of the low transfer rate of nitrogen and oxygen through membrane and the relatively large velocity at the cathode.

2.6 Purge process

As mentioned above, the performance of DEA-PEMFC would decrease over the time. To restore the cell performance, the anode outlet is open for a short time to clear the internal impurities. This operation is also known as purge. During the purge process, the PEMFC actually works at the FTA mode. The alternating DEA mode and FTA mode is executed by a solenoid valve.

In this numerical model, DEA mode is implemented by setting the outlet boundary condition as wall, while FTA mode is implemented by setting the outlet boundary condition as pressure outlet. To simulate the working process of the solenoid valve, a journal file is employed to change boundary conditions automatically. The flowchart is displayed in Fig. S2. This journal file is able to change the boundary conditions according to voltage drop or duration.

2.7 Boundary conditions

For the steady calculation, mass flow rate boundary condition is applied at both the anode inlet and the cathode inlet. The mass flow rate is calculated with Eq. (28).

$$m_a = \frac{\rho_a \xi_a RTi_{ref} A_{act}}{2FP_a x_{H_2}}, \qquad m_c = \frac{\rho_c \xi_c RTi_{ref} A_{act}}{4FP_c x_{O_2}} \tag{28}$$

where ξ is the stoichiometry ratio; i_{ref} is the reference current density (A/m^2), which is set to 1 A/cm^2; A_{act} is the effective membrane area (m^2).

For the transient calculation, pressure inlet boundary condition is applied at the anode inlet. Besides, the boundary condition at the anode outlet is controlled by the journal file mentioned above.

The constant temperature boundary condition is set at the anode inlet and the cathode inlet. The mole fraction of vapor at the anode inlet and the cathode inlet is calculated with Eq. (29).

$$x_{\mathrm{H_2O,a}} = \frac{P_{\mathrm{sat}} RH_{\mathrm{a}}}{P_{\mathrm{a}}}, \qquad x_{\mathrm{H_2O,c}} = \frac{P_{\mathrm{sat}} RH_{\mathrm{c}}}{P_{c}} \tag{29}$$

where RH denotes the relative humidity.

3 Model validation

3.1 Model implement

The computation domain of DEA-PEMFC is shown in Fig. S3(a). This geometry is divided into nine regions. Besides, structural grid is employed for spatial discretization in all the regions, as shown in Fig. S3(b). The corresponding geometry and operating parameters are listed in Table 2 [42].

Table 2. The geometry and operating parameters used in the model [42].

Parameter	Value
Length of PEMFC	50 mm
Width of PEMFC	0.95 mm
Height of gas channel	1 mm
Thickness of GDL	0.3 mm
Thickness of CL	0.0129 mm
Thickness of membrane	0.06 mm
Stoichiometry ratio of hydrogen and air	3/3
Inlet pressure at the anode	0.0005 atm
Inlet temperature at the anode and the cathode	298.15 K/328.15 K
Relative humidity at the anode and the cathode	0/1.0
Operating temperature	338.15 K

This model is solved by software Fluent (ANSYS Inc., USA). The build-in mass conservation equation, momentum conservation equation, species transport equation, and energy conservation equation are employed to present the fluid flow, species transport, and temperature distribution. In the meanwhile, the electronic charge conservation equation, ionic charge conservation equation, dissolved water transport equation, and liquid water transport equation are defined by the user-defined scalar. The corresponding terms in these equations are defined by

the user-defined function. At the beginning of each case, the steady model is solved. Then, the steady solution is served as initial conditions for the transient calculation. This procedure is also beneficial to improve the model convergence.

3.2 Model validation

The grid number has a significant influence on the simulation results. Herein, the gird independence for the steady and transient cases is carried out first, as seen in Fig. S4. The used grid number ranges from 60000 to 250000. It is found that when the grid number decreases from 123500 to 65000, the voltage for the steady case reduces sharply from 0.577 V to 0.566 V. Meanwhile, under the grid number of 65000, the voltage variation for the transient case is also quite different from that under the grid number of 123500 and 247000, as seen in Fig. S4(b). Under the grid number of 123500 and 247000, the voltage has a slow reduction first and then a fast reduction, while that has an approximately linear decrease under the grid number of 65000. Therefore, considering both the calculation accuracy and the calculation time, the grid number of 123500 is used for the following simulation.

The comparison between simulation results and experiment data is displayed in Fig. 2. For the steady case, the simulation results agree well with the experiment data [42], as seen in Fig. 2(a). Although only three data points are provided in the experiment, the three points cover the commonly used operating range. Besides, according to the comprehensive model validation of PEMFC in our previous work [29], the position of the polarization curve could be determined well by the three data points. For the transient cases, the simulation results under a low current density also have a good agreement with the experiment data [42], as seen in Fig. 2(b). Under the high current density of 8000 A/m^2, an error exists between the simulation results and experiment data. This may be attributed to the model simplification and the errors in the model parameter estimation. Nevertheless, in the practical application, the selected operating current density are generally smaller than 8000 A/m^2, considering other effects. On the other hand, the purge interval would not be too long, in order to avoid large performance drop. Therefore, the existing error under the operating current density of 8000 A/m^2 has a small impact on the analysis conclusions.

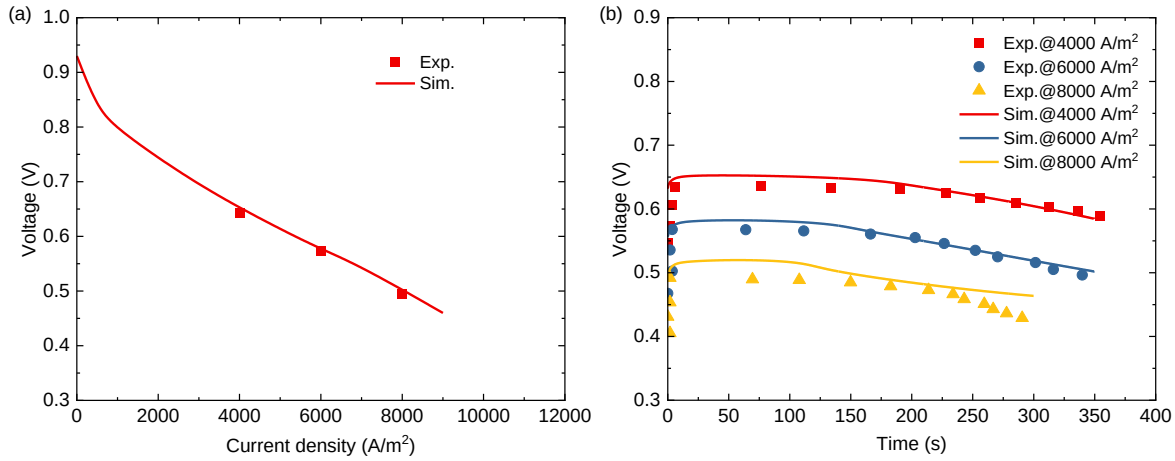

Fig. 2. The comparison between simulation results and experiment data [42]: (a) the steady cases; (b) the transient cases.

4 Results and discussion

4.1 Effects of current density

Current density is an important operating parameter for DEA-PEMFC. The steady electrical-thermal-water performance under different current densities is presented in Fig. 3. The voltage is decreased with the increasing current density, as seen in Fig. 3(a), because the overvoltage is risen. The maximum temperature also increases with the increasing current density, as seen in Fig. 3(b). It should be noted that the temperature rise inside PEMFC maintains at a low value. This is because constant temperature boundary condition is applied in this model, which represents the strong heat transfer performance. With the increase of current density, the heat taken away by the fluid in the channel is almost the same, while the heat dissipation through the cathode current collector becomes more and more significant. As for liquid water, the flow rate of liquid water is quite small, as seen in Fig. 3(c). In these cases, the mole fraction of vapor is lower than the saturation value (about 24% for the operating temperature of 338.15 K at the atmospheric pressure). Thus, it could be concluded that nearly all the liquid water evaporates, leading to the small flow rate of liquid water.

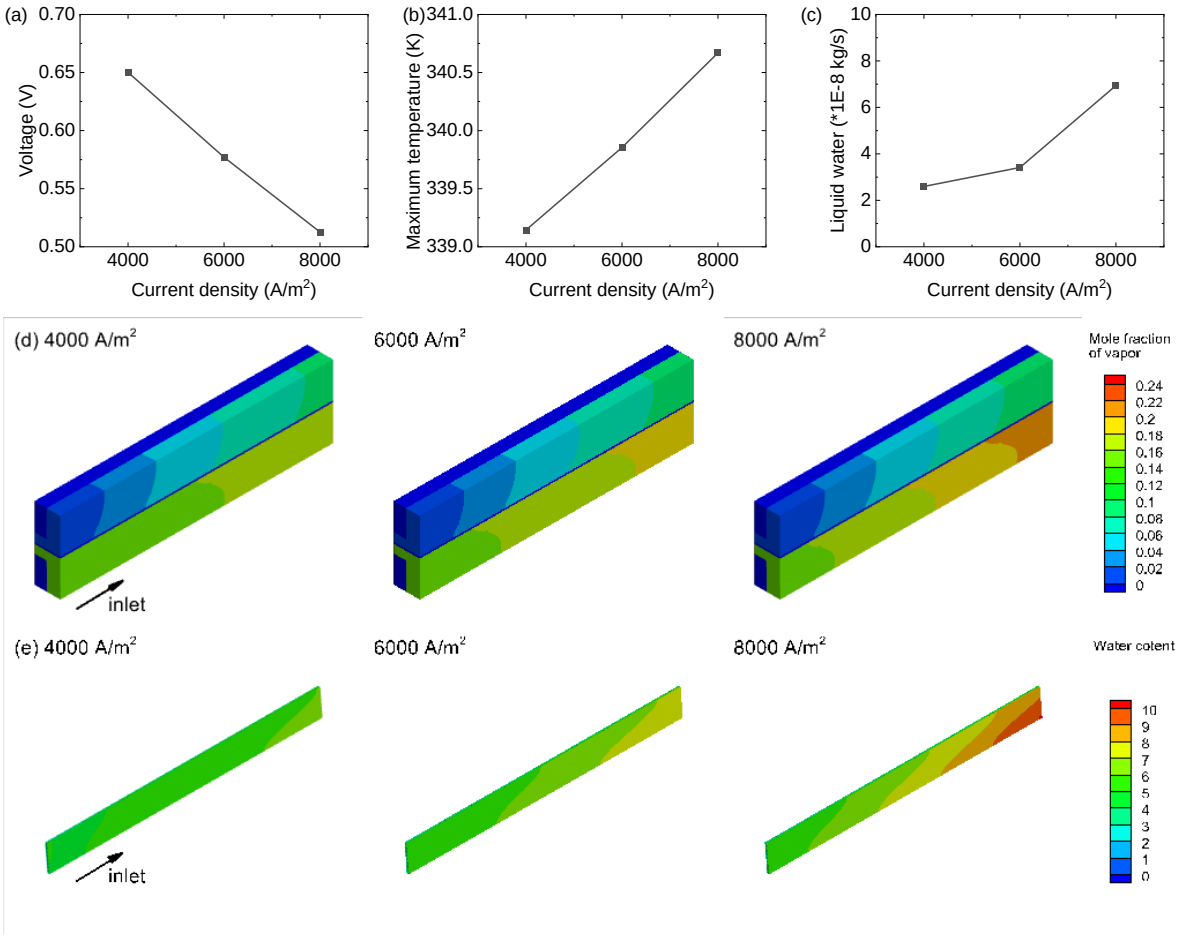

Fig. 3. (a) The voltage, (b) maximum temperature, and (c) flow rate of liquid water under different current densities; the distributions of (d) the mole fraction of vapor and (e) water content under different current densities.

The transient voltage under different current densities is presented in Fig. 4(a). The voltage-time curve could be divided into three stages according to its trend. At the beginning, the voltage has a small increase, because the anode outlet is closed during the transient calculation, thus reducing water evaporation from the membrane and raising the water content in the membrane. Next, the voltage has a slight decrease due to the nitrogen and oxygen accumulation at the anode. These impurities gradually accumulate at the position close to anode outlet, decreasing the hydrogen concentration for electrochemical reaction. Nevertheless, electrochemical reaction is not very sensitive to hydrogen concentration, resulting in the slow decrease rate in this stage. Then, the reduction rate of voltage becomes large in the third stage. Different from the second stage, the hydrogen concentration at the position close to anode outlet decreases to very small value in this stage, so that the electrochemical reaction at this position almost stops. Therefore, the voltage is remarkably affected by the accumulation of nitrogen and oxygen in this stage.

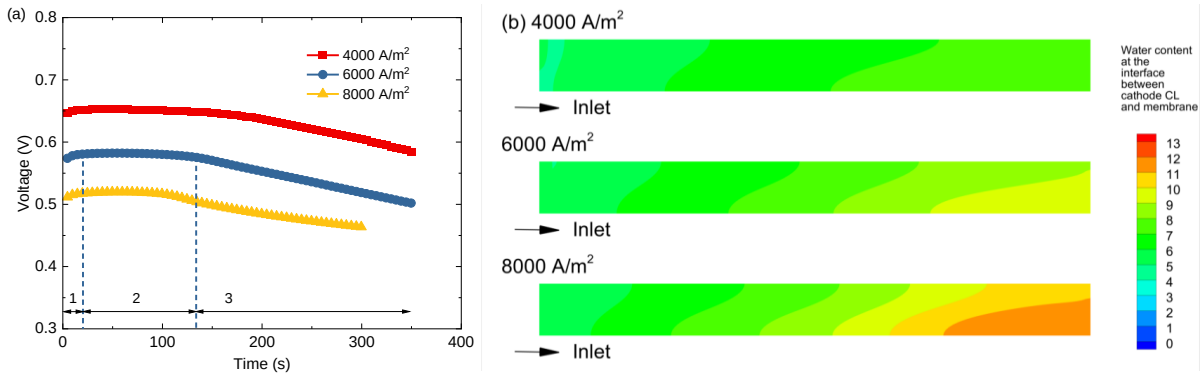

Fig. 4. (a) The voltage variation of DEA-PEMFC over time and (b) the distribution of the water content at the interface between cathode CL and membrane at 100 s under different current densities.

Under a high current density, the duration of the second stage is shorter than that under a low current density. This phenomenon shows the high crossover rate of nitrogen and oxygen under the high current density. In this condition, the high electrochemical reaction rate would generate more water, thus increasing the water content in the membrane and raising the crossover rate, as seen in Fig. 4(b). Correspondingly, it is also found that the voltage drop rate in the third stage become faster when the operating current density is increased from 4000 A/m^2 to 6000 A/m^2. Nevertheless, when the current density is increased further to 8000 A/m^2, the voltage drop rate is fast first and then slow in this stage.

The distribution variations of the current density and overvoltage inside DEA-PEMFC over time are presented in Fig. 5. As seen in Fig. 5(a), at the beginning of calculation (20 s), the current density is first increased along the flow direction, and then decreased till the end of channel. Therefore, the maximum value of current density appears at the middle of DEA-PEMFC along the flow direction. The current density is mainly dominated by the reactant concentration and the resistance of membrane. At the position close to inlet, the reactant concentration is large, and the absolute value of overvoltage is small, as seen in Fig. 5(b). However, at this position, the low water content in the membrane increases the membrane resistance, resulting in the low current density. By contrast, at the position

close to outlet, the water content in the membrane is large. However, the reactant concentration is low, and the absolute value of overvoltage is also relatively large, decreasing the current density.

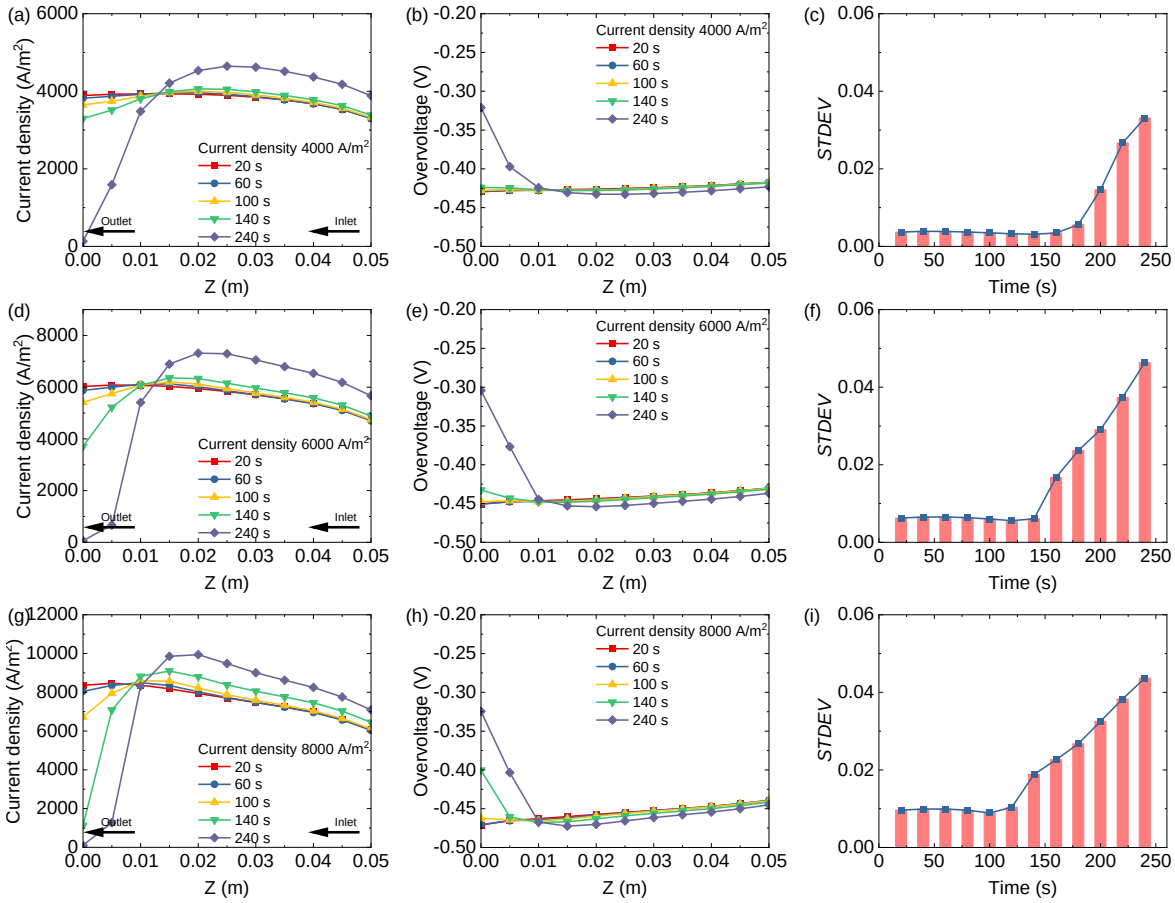

Fig. 5. The distribution variations of the current density at the middle of membrane (a, d, g) and the overvoltage at the cathode CL (b, e, h) over time under different current densities; the variation of the *STDEV* of overvoltage over time (c, f, i) under different current densities.

As the time moves forward, the current density at the position close to outlet decreases significantly, as seen in Fig. 5(a). At 240 s, the current density at the outlet is quite close to zero. This is because of the accumulation of nitrogen and oxygen at the anode outlet, decreasing the hydrogen concentration. Correspondingly, the absolute value of overvoltage at this position is also decreased, which increases the risk of local carbon corrosion. Besides, it is also found that the current density at the position close to inlet is improved. When the time goes from 20 s to 240 s, the maximum current density is risen from 3933 A/m^2 to 4646 A/m^2 under the working current density of 4000 A/m^2, increased by 18%. On the whole, the crossover of nitrogen and oxygen tends to aggravate the non-uniformity in DEA-PEMFC with the increase of time. However, in Fig. 5(c), the results show that the *STDEV* of overvoltage could have a slight decrease first and then a fast increase. When the DEA-PEMFC is operated at 4000 A/m^2, the minimum value appears at about 140 s.

With the increase of working current density, the low current density region at the same instant significantly expands. Nevertheless, under different working current densities, the affected area (where current density is lower

than that in the steady solution) by impurities at the anode is quite close, as shown in Fig. 5. As for the non-uniformity, the *STDEV* of overvoltage at a high working current density is higher than that at a low working current density at the same instant. Meanwhile, the minimum value of *STDEV* comes early at the high working current density. Under the working current density of 6000 and 8000 A/m^2, the turning point appears at about 100-120 s.

4.2 Effects of operating temperature

The operating temperature affects the electrochemical reaction rate and the phase change of water. The steady performance under different operating temperatures is displayed in Fig. S5. With the increase of operating temperature, the corresponding voltage decreases. Although the high operating temperature raises the electrochemical reaction activity, it also accelerates the evaporation of liquid water, which reduces the water content in the membrane and increases the resistance, as seen in Fig. S5(d) and (e). The maximum temperature is still quite close to operating temperature. Hence, the maximum temperature changes linearly with the operating temperature. Also, the flow rate of liquid water is decreased with the increase of operating temperature.

The transient performance under different operating temperatures is presented in Fig. 6(a). Under a high operating temperature, the water content in the membrane is low, as seen in Fig. 6(b), which would suppress the crossover of nitrogen and oxygen. However, according to Eq. (25) and (26), the high temperature could also increase the crossover rate. Therefore, in these cases, temperature has both positive and negative effects on the crossover rate. When temperature is increased from 328.15 K to 338.15 K, the crossover rate of nitrogen and oxygen almost keeps the same. The voltage-time curves under the temperature of 328.15 and 338.15 K are almost parallel. While increasing temperature to 348.15 K further, faster voltage drop is observed. At about 345 s, the voltage drop under 348.15 K achieves 0.1 V, thus the calculation is stopped.

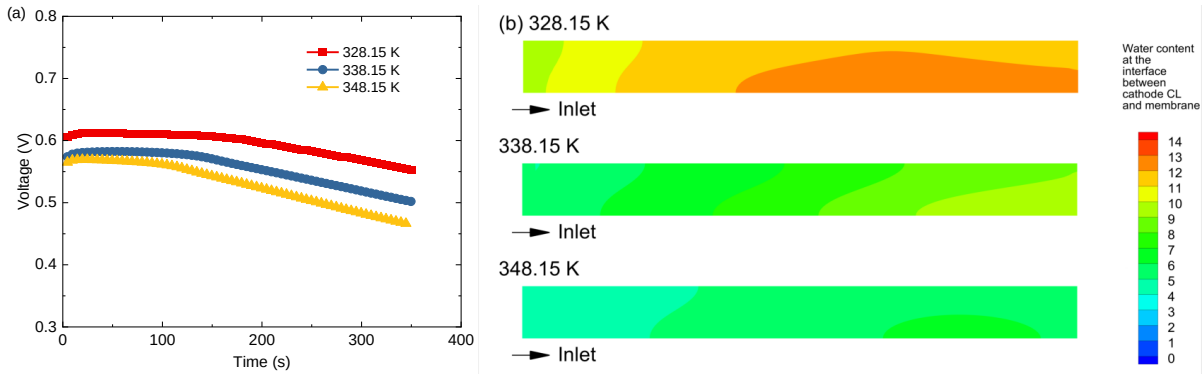

Fig. 6. (a) The voltage variation of DEA-PEMFC over time and (b) the distribution of the water content at the interface between cathode CL and membrane at 100 s under different operating temperatures.

The distribution of current density at the middle of membrane under different operating temperatures is displayed in Fig. S6. At the beginning of the transient calculation (20 s), in the *x*-axis direction, the current density at the position below the current collector is higher than that below the channel. In the *z*-axis direction, the current density at the inlet and outlet is quite close. Hence, the maximum current density appears at the middle of DEA-

PEMFC. At this position, both the water content and reactant concentration maintain at a relatively high level. With the increase of time, the current density at the outlet becomes lower than that at the inlet gradually. In addition, low current density region close to outlet expands over time. By contrast, the current density at the inlet is increased. This is because the crossover of nitrogen and oxygen reduces the electrochemical reaction rate at the outlet, thus aggravating the non-uniformity inside DEA-PEMFC.

At the low temperature of 328.15 K, the extremely low current density appears in the range of 140-240 s. Increasing temperature to 348.15 K further, the emergence of extremely low current density becomes earlier considering the relatively large low current density region at 140 s. Hence, it could be concluded that high temperature would accelerate the emergence of the low current density region at the position close to outlet. Meanwhile, the decrease of current density also becomes quicker with the raise of operating temperature. The affected area by the crossover of nitrogen and oxygen becomes large as the temperature increases. Besides, under the same working current density (6000 A/m^2), it is found that the current density at the position close to inlet becomes higher with the increase of operating temperature.

4.3 Effects of cathode stoichiometry ratio

DEA mode is generally used for air-cooled PEMFC where the stoichiometry ratio at the cathode is quite large. In order to approximate the actual working conditions, the effects of cathode stoichiometry ratio on the DEA-PEMFC performance are discussed in this section.

The steady performance under various stoichiometry ratios is presented in Fig. S7. It is found that the voltage only has a small reduction with the stoichiometry ratio increasing from 3 to 12 in this study. Correspondingly, the maximum temperature is also reduced a bit. Under a high cathode stoichiometry ratio, the mole fraction of vapor at the cathode is decreased, especially at the position close to outlet, as seen in Fig. S7(e). Hence, the water content in the membrane is reduced, and the resistance of membrane is risen, which would decrease PEMFC performance. Nevertheless, the high stoichiometry ratio also increases the oxygen concentration at the cathode, as seen in Fig. S7(d). Thus, performance degradation of PEMFC is alleviated significantly. In addition, the flow rate of liquid water is still small.

The transient voltage variation under different stoichiometry ratios is presented in Fig. 7. The cathode stoichiometry ratio has a relatively slight effect on the DEA-PEMFC performance. In the second stage, when DEA-PEMFC is operated under a low stoichiometry ratio (about 3), the output voltage is raised to a high level (more than 0.58 V). At the meantime, the duration of the second stage under a low stoichiometry ratio is a little shorter than that under a high stoichiometry ratio. On the other hand, in the third stage, the voltage drop rate under the stoichiometry ratio of 3 is faster than that under a high stoichiometry ratio. Within 350 s, the output voltage under the stoichiometry ratio of 3 achieves the lowest value, about 0.5 V. This is attributed to water content variation under different stoichiometry ratios, as seen in Fig. 7(b). Under the low stoichiometry ratio, the large water content in the membrane leads to high crossover rate of nitrogen and oxygen. By contrast, under the high stoichiometry

ratio, more water is taken away by the air at the cathode. In this condition, the water content in the membrane is hard to increase, and the crossover rate of nitrogen and oxygen is small, resulting in the slow voltage drop rate.

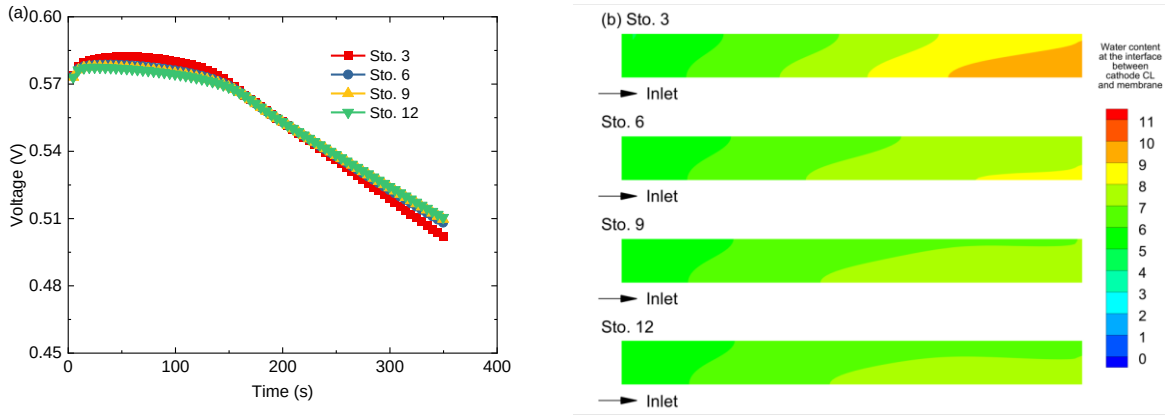

Fig. 7. (a) The voltage variation over time and (b) the distribution of the water content at the interface between cathode CL and membrane at 100 s under different cathode stoichiometry ratios.

The distribution of variables along the flow direction under different stoichiometry ratios is displayed in Fig. S8. The current density at the position close to outlet is reduced over time. Under a high stoichiometry ratio, the current density has a small reduction rate. At 240 s, the current density at the position close to outlet (Z = 0.005 m) under a high stoichiometry ratio is larger than that under a low stoichiometry ratio. Correspondingly, the overvoltage at the position close to outlet is decreased as the stoichiometry ratio increasing. This is because of the low impurity concentration at the anode under the high stoichiometry ratio. At the position close to inlet, the current density is increased over time due to the same operating current density. Nevertheless, the current density under the high stoichiometry ratio has a smaller increase than that under the low stoichiometry ratio at the same instant. Under the stoichiometry ratio of 12, the increase of the maximum current density from 20 s to 240 s is 16.7%, while that achieves 20.3% under the stoichiometry ratio of 3.

Besides, the *STDEV* of overvoltage is also calculated in Fig. S8. Similarly, the *STDEV* of overvoltage under all the stoichiometry ratios is reduced first and then increased fast. However, some differences could be also found. The *STDEV* of overvoltage under a low stoichiometry ratio is larger than that under a high stoichiometry ratio at the same instant. Furthermore, the high stoichiometry ratio helps to maintain the *STDEV* of overvoltage at a low value for a long time. That's to say, the high stoichiometry ratio enables to delay the increase of the *STDEV* of overvoltage. In these cases, the minimum value of the *STDEV* of overvoltage appears at about 120 s.

4.4 The purge optimization

Based on the above-mentioned analysis, it could be concluded that the *STDEV* of overvoltage is reduced first and then increased fast under all the cases. Furthermore, the decrease mainly appears in the first and second stage. Hence, to avoid the irreversible damage to PEMFC, the purge interval should be also included in the first and

second stage. Meanwhile, to improve the utilization of hydrogen, the purge interval should be large. That's to say, the start time of purge should be near the end of the second stage.

Herein, the purge strategy is optimized based on the non-uniformity of overvoltage. The purge interval is determined to 100 s according to the *STDEV* of overvoltage in these cases. After 100 s, the *STDEV* of overvoltage would become large under the operating current density of 8000 A/m^2. This purge interval is suitable for almost all the cases discussed above (working conditions: current density of 4000-8000 A/m^2, operating temperature of 328.15-348.15 K, cathode stoichiometry ratio of 3-12, and anode relative humidity of zero).

Based on the optimal purge interval of 100 s, the purge duration is also optimized to achieve stable output performance. The voltage variation over time under the purge duration of 0.6 and 0.2 s is presented in Fig. 8(a). Before the purge of each cycle, the voltage is decreased to 0.5802 V. At the beginning of purge, the voltage is first increased to a high level (0.5893 V), which is the maximum value of the cycle. This is because the fast removal of impurities increases the performance of DEA-PEMFC. Afterwards, the voltage would decrease till the purge is completed. During this time period, the hydrogen at the low temperature and humidity reduces the water content in the membrane further, thus leading to performance deterioration. Besides, during the purge interval, the mole fraction of nitrogen at the anode achieves about 10%, as seen in Fig. 8(b). It is also found that the mole fraction of nitrogen changes linearly with time.

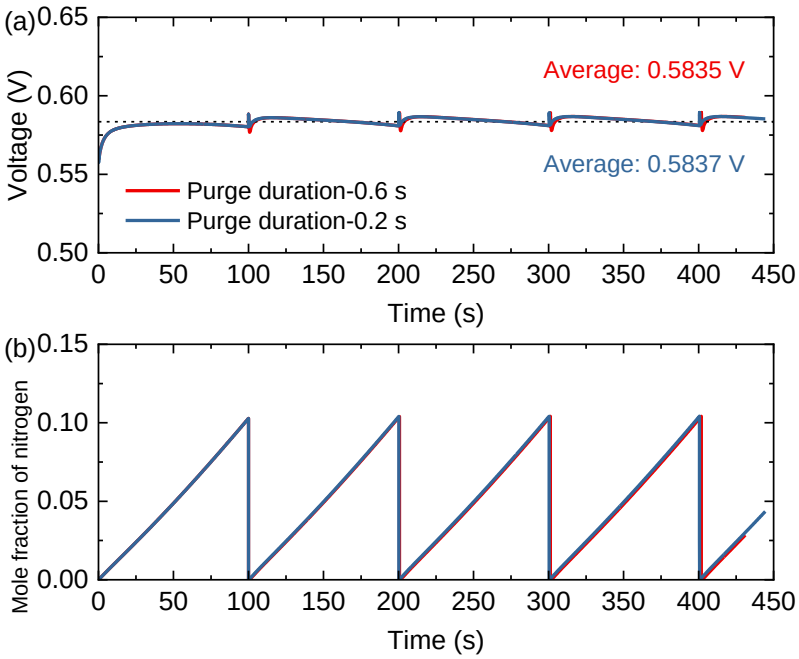

Fig. 8. The variation of (a) voltage and (b) the mole fraction of nitrogen at the anode over time.

Under the purge duration of 0.6 s, the voltage decreases to minimum value (0.5774 V) at the end of purge, decreasing by 2.02% compared with the maximum value. By comparison, under the purge duration of 0.2 s, the minimum voltage is decreased by 0.95% compared with the maximum voltage. Hence, the purge duration of 0.2 s

is beneficial to improve the hydrogen utilization (over 99%) and achieve a stable output performance. On the whole, this purge optimization could achieve a good voltage stability of DEA-PEMFC.

5 Conclusions

In this paper, a 3D transient model of DEA-PEMFC integrated with the crossover of nitrogen and oxygen is developed to describe the internal species transport behaviors and electrochemical reaction process. Then, the effects of operating parameters on the uneven electrical-thermal-water performance are investigated. Finally, a purge optimization is carried out based on the uneven distribution of field variables to achieve the high stability of DEA-PEMFC. The conclusions could be drawn as follows:

(1) During the steady process, the voltage of PEMFC is reduced with the raise of working current density, operating temperature, and cathode stoichiometry ratio. In the scope of this study, the working current density and operating temperature have more significant effects on the PEMFC voltage than the cathode stoichiometry ratio. The temperature rise inside PEMFC is small due to the strong heat transfer capacity of current collector. Besides, the flow rate of liquid water is also small (on the order of 1e-8 kg/s) for these cases.

(2) During the transient process, the voltage-time curve could be divided into three stages according to its trend. In the second and third stage, the voltage of DEA-PEMFC has a faster reduction over time under the higher current density or operating temperature. In the meanwhile, the duration of the second stage is shorter under the higher current density or operating temperature. Besides, it is also found that the current density at the position close to outlet is reduced, while that at the position close to inlet is raised over the time.

(3) On the whole, the crossover of nitrogen and oxygen would aggravate the non-uniformity of DEA-PEMFC. It is found that the *STDEV* of overvoltage is reduced first and then increased fast over time in the scope of this study. The minimum *STDEV* of overvoltage appears near the end of the second stage (at 100-140 s). Hence, purge at this moment is beneficial to avoid the irreversible damage to DEA-PEMFC.

(4) Based on the analysis, the purge strategy is optimized to achieve high stability of DEA-PEFMC. The purge interval is determined to 100 s, which is suitable for almost all the discussed cases (working conditions: current density of 4000-8000 A/m^2, operating temperature of 328.15-348.15 K, cathode stoichiometry ratio of 3-12, and anode relative humidity of zero). The purge duration is reduced to 0.2 s. In this condition, the minimum voltage is reduced by about 0.95% compared with the maximum value, indicating a good voltage stability.

Acknowledgments

This work was financially supported by the National Key R&D Program of China (2022YFE0101300), the National Natural Science Foundation of China (52176203), the Key R&D Project of Shaanxi Province, China (2023-GHZD-13), and the “Young Talent Support Plan” of Xi’an Jiaotong University (QB-A-JZB2015004).

References

[1] A. Thakur, D. Ghosh, P. Devi, K.-H. Kim, P. Kumar, Current progress and challenges in photoelectrode materials for the production of hydrogen, Chemical Engineering Journal, 397 (2020) 125415.

[2] J. Lee, S. Ga, D. Lim, S. Lee, H. Cho, J. Kim, Carbon-free green hydrogen production process with induction heating-based ammonia decomposition reactor, Chemical Engineering Journal, 457 (2023) 141203.

[3] J. Yao, Z. Wu, H. Wang, F. Yang, J. Xuan, L. Xing, J. Ren, Z. Zhang, Design and multi-objective optimization of low-temperature proton exchange membrane fuel cells with efficient water recovery and high electrochemical performance, Applied Energy, 324 (2022) 119667.

[4] Ö. Atlam, G. DÜNdar, A practical Equivalent Electrical Circuit model for Proton Exchange Membrane Fuel Cell (PEMFC) systems, International Journal of Hydrogen Energy, 46 (2021) 13230-13239.

[5] Y. Xu, G. Chang, R. Fan, T. Cai, Effects of various operating conditions and optimal ionomer-gradient distribution on temperature-driven water transport in cathode catalyst layer of PEMFC, Chemical Engineering Journal, 451 (2023) 138924.

[6] P. Koski, J. Viitakangas, J. Ihonen, Determination of fuel utilisation and recirculated gas composition in dead-ended PEMFC systems, International Journal of Hydrogen Energy, 45 (2020) 23201-23226.

[7] Z. Du, Q. Liu, X. Wang, L. Wang, Performance investigation on a coaxial-nozzle ejector for PEMFC hydrogen recirculation system, International Journal of Hydrogen Energy, 46 (2021) 38026-38039.

[8] S. Liu, T. Chen, C. Zhang, Y. Xie, Study on the performance of proton exchange membrane fuel cell (PEMFC) with dead-ended anode in gravity environment, Applied Energy, 261 (2020) 114454.

[9] X. Yu, X. Luo, Z. Tu, Development of a compact high-power density air-cooled proton exchange membrane fuel cell stack with ultrathin steel bipolar plates, Energy, 270 (2023) 126936.

[10] Y. Yang, X. Zhang, L. Guo, H. Liu, Local degradation in proton exchange membrane fuel cells with dead-ended anode, Journal of Power Sources, 477 (2020) 229021.

[11] J.C. Kurnia, A.P. Sasmito, T. Shamim, Advances in proton exchange membrane fuel cell with dead-end anode operation: A review, Applied Energy, 252 (2019) 113416.

[12] A. Manokaran, S. Pushpavanam, P. Sridhar, S. Pitchumani, Experimental analysis of spatio-temporal behavior of anodic dead-end mode operated polymer electrolyte fuel cell, Journal of Power Sources, 196 (2011) 9931-9938.

[13] S. Xu, B. Yin, Z. Li, F. Dong, A review on gas purge of proton exchange membrane fuel cells: Mechanisms, experimental approaches, numerical approaches, and optimization, Renewable and Sustainable Energy Reviews, 172 (2023) 113071.

[14] Q. Jian, L. Luo, B. Huang, J. Zhao, S. Cao, Z. Huang, Experimental study on the purge process of a proton exchange membrane fuel cell stack with a dead-end anode, Applied Thermal Engineering, 142 (2018) 203-214.

[15] A.P. Sasmito, M.I. Ali, T. Shamim, A Factorial Study to Investigate the Purging Effect on the Performance of a Dead-End Anode PEM Fuel Cell Stack, Fuel Cells, 15 (2015) 160-169.

[16] Z. Hu, Y. Yu, G. Wang, X. Chen, P. Chen, J. Chen, S. Zhou, Anode purge strategy optimization of the polymer electrode membrane fuel cell system under the dead-end anode operation, Journal of Power Sources, 320 (2016) 68-77.

[17] J. Shen, C. Du, F. Yan, B. Chen, Z. Tu, Experimental study on the dynamic performance of a power system with dual air-cooled PEMFC stacks, Applied Energy, 326 (2022) 120025.

[18] L. Fan, Y. liu, X. Luo, Z. Tu, S.H. Chan, A novel gas supply configuration for hydrogen utilization improvement in a multi-stack air-cooling PEMFC system with dead-ended anode, Energy, 282 (2023) 129004.

[19] B. Wang, H. Deng, K. Jiao, Purge strategy optimization of proton exchange membrane fuel cell with anode recirculation, Applied Energy, 225 (2018) 1-13.

[20] B. Chen, H. Zhou, S. He, K. Meng, Y. Liu, Y. Cai, Numerical simulation on purge strategy of proton exchange membrane fuel cell with dead-ended anode, Energy, 234 (2021) 121265.

[21] R. Fan, G. Chang, Y. Xu, J. Xu, Multi-objective optimization of graded catalyst layer to improve performance and current density uniformity of a PEMFC, Energy, 262 (2023) 125580.

[22] X. Yu, Y. Liu, Z. Tu, S.H. Chan, Endplate effect in an open-cathode proton exchange membrane fuel cell stack: Phenomenon and resolution, Renewable Energy, 219 (2023) 119392.

[23] A.P. Sasmito, A.S. Mujumdar, Performance evaluation of a polymer electrolyte fuel cell with a dead-end anode: A computational fluid dynamic study, International Journal of Hydrogen Energy, 36 (2011) 10917-10933.

[24] J.P. Meyers, R.M. Darling, Model of Carbon Corrosion in PEM Fuel Cells, Journal of The Electrochemical Society, 153 (2006) A1432.

[25] G. Zhang, L. Fan, J. Sun, K. Jiao, A 3D model of PEMFC considering detailed multiphase flow and anisotropic transport properties, International Journal of Heat and Mass Transfer, 115 (2017) 714-724.

[26] G. Zhang, K. Jiao, Three-dimensional multi-phase simulation of PEMFC at high current density utilizing Eulerian-Eulerian model and two-fluid model, Energy Conversion and Management, 176 (2018) 409-421.

[27] G. Zhang, B. Xie, Z. Bao, Z. Niu, K. Jiao, Multi-phase simulation of proton exchange membrane fuel cell with 3D fine mesh flow field, International Journal of Energy Research, 42 (2018) 4697-4709.

[28] L. Xing, P.K. Das, X. Song, M. Mamlouk, K. Scott, Numerical analysis of the optimum membrane/ionomer water content of PEMFCs: The interaction of Nafion® ionomer content and cathode relative humidity, Applied Energy, 138 (2015) 242-257.

[29] J. Yao, Y. Yang, X. Hou, Y. Yang, F. Yang, Z. Wu, Z. Zhang, Fast design of catalyst layer with optimal electrical-thermal-water performance for proton exchange membrane fuel cells, Journal of Energy Chemistry, 81 (2023) 642-655.

[30] X. Yu, S. Cai, X. Luo, Z. Tu, Barrel effect in an air-cooled proton exchange membrane fuel cell stack, Energy, 286 (2024) 129668.

[31] G. Zhang, J. Wu, Y. Wang, Y. Yin, K. Jiao, Investigation of current density spatial distribution in PEM fuel cells using a comprehensively validated multi-phase non-isothermal model, International Journal of Heat and Mass Transfer, 150 (2020).

[32] Q. Ding, K.-Q. Zhu, C. Yang, X. Chen, Z.-M. Wan, X.-D. Wang, Performance investigation of proton exchange membrane fuel cells with curved membrane electrode assemblies caused by pressure differences between cathode and anode, International Journal of Hydrogen Energy, 46 (2021) 37393-37405.

[33] Q. Wang, F. Tang, B. Li, H. Dai, J.P. Zheng, C. Zhang, P. Ming, Study on the thermal transient of cathode catalyst layer in proton exchange membrane fuel cell under dynamic loading with a two-dimensional model, Chemical Engineering Journal, 433 (2022) 133667.

[34] L. Fan, G. Zhang, K. Jiao, Characteristics of PEMFC operating at high current density with low external humidification, Energy Conversion and Management, 150 (2017) 763-774.

[35] X.-G. Yang, Q. Ye, P. Cheng, Matching of water and temperature fields in proton exchange membrane fuel cells with non-uniform distributions, International Journal of Hydrogen Energy, 36 (2011) 12524-12537.

[36] W. Sun, B.A. Peppley, K. Karan, An improved two-dimensional agglomerate cathode model to study the influence of catalyst layer structural parameters, Electrochimica Acta, 50 (2005) 3359-3374.

[37] N. Khajeh-Hosseini-Dalasm, M.J. Kermani, D.G. Moghaddam, J.M. Stockie, A parametric study of cathode catalyst layer structural parameters on the performance of a PEM fuel cell, International Journal of Hydrogen Energy, 35 (2010) 2417-2427.

[38] L. Xing, Y. Xu, Ž. Penga, Q. Xu, H. Su, F. Barbir, W. Shi, J. Xuan, A segmented fuel cell unit with functionally graded distributions of platinum loading and operating temperature, Chemical Engineering Journal, 406 (2021) 126889.

[39] L. Xing, X. Liu, T. Alaje, R. Kumar, M. Mamlouk, K. Scott, A two-phase flow and non-isothermal agglomerate model for a proton exchange membrane (PEM) fuel cell, Energy, 73 (2014) 618-634.

[40] O.B. Rizvandi, S. Yesilyurt, A pseudo three-dimensional, two-phase, non-isothermal model of proton exchange membrane fuel cell, Electrochimica Acta, 302 (2019) 180-197.

[41] R.K. Ahluwalia, X. Wang, Buildup of nitrogen in direct hydrogen polymer-electrolyte fuel cell stacks, Journal of Power Sources, 171 (2007) 63-71.

[42] Y.-S. Chen, C.-W. Yang, J.-Y. Lee, Implementation and evaluation for anode purging of a fuel cell based on nitrogen concentration, Applied Energy, 113 (2014) 1519-1524.